Journal of Advanced Ceramics
2023, **12**(8): 1511–1520
https://doi.org/10.26599/JAC.2023.9220768
ISSN 2226-4108
CN 10-1154/TQ

Research Article

Superior multiphase interfaces in AgCuTe-based composite with significantly enhanced thermoelectric properties

Wenpei Li[a,†], Zhonghai Yu[a,†], Chengyan Liu[a,*], Ying Peng[b], Baoquan Feng[a], Jie Gao[a], Guojing Wu[a], Xiaobo Bai[a], Junliang Chen[a], Xiaoyang Wang[a], Lei Miao[a,*]

[a]*Guangxi Key Laboratory of Information Materials*, *Electronical Information Materials and Devices Engineering Research Center of Ministry of Education*, *School of Materials Science and Engineering*, *Guilin University of Electronic Technology*, *Guilin 541004*, *China*
[b]*Guangxi Key Laboratory of Precision Navigation Technology and Application*, *School of Information and Communication*, *Guilin University of Electronic Technology*, *Guilin 541004*, *China*

Received: March 31, 2023; Revised: May 2, 2023; Accepted: May 18, 2023

Abstract: It is common sense that a phase interface (or grain boundary) could be used to scatter phonons in thermoelectric (TE) materials, resulting in low thermal conductivity (κ). However, a large number of impurity phases are always so harmful to the transport of carriers that poor TE performance is obtained. Here, we demonstrate that numerous superior multiphase (AgCuTe, Ag_2Te, copper telluride (Cu_2Te and $Cu_{2-x}Te$), and nickel telluride (NiTe)) interfaces with simultaneous strong phonon scattering and weak electron scattering could be realized in AgCuTe-based TE materials. Owing to the similar chemical bonds in these phases, the depletion region at phase interfaces, which acts as carrier scattering centers, could be ignored. Therefore, the power factor (PF) is obviously enhanced from ~609 to ~832 $\mu W \cdot m^{-1} \cdot K^{-2}$, and κ is simultaneously decreased from ~0.52 to ~0.43 $W \cdot m^{-1} \cdot K^{-1}$ at 636 K. Finally, a peak figure of merit (zT) of ~1.23 at 636 K and an average zT (zT_{avg}) of ~1.12 in the temperature range of 523–623 K are achieved, which are one of the best values among the AgCuTe-based TE materials. This study could provide new guidance to enhance the performance by designing superior multiphase interfaces in the TE materials.

Keywords: thermoelectric (TE) materials; AgCuTe; phase interface; carrier scattering; phonon scattering

1 Introduction

Thermoelectric (TE) materials can be used to convert low-quality heat into high-quality electricity through all-solid-state and environmentally friendly methods, attracting significant attention in the past decades [1,2]. To be a competitor with traditional power generators, the energy conversion efficiency of the TE materials needs to be improved, which is generally evaluated by the figure of merit (zT) [3]. High zT at the operating temperature leads to high energy conversion efficiency, and hence the TE materials with high Seebeck coefficient (S) and electrical conductivity (σ), and low

† Wenpei Li and Zhonghai Yu contributed equally to this work.
* Corresponding authors.
E-mail: C. Liu, chengyanliu@guet.edu.cn;
L. Miao, miaolei@guet.edu.cn

thermal conductivity (κ) are promising candidates according to the equation: $zT = S^2\sigma T/\kappa$, where T is the absolute temperature. However, not only S, σ, and carrier thermal conductivity (κ_e) are strongly related to the carrier concentration (n) [4], but also the electron and phonon transport is always blocked at the same scattering center, such as grain boundary or phase interface [5], so that this coupling restricts the further improvement of zT.

To decouple the electron and phonon transport, the concepts of "phonon-glass electron-crystal" (PGEC) [6] and the following "phonon-liquid electron-crystal" (PLEC) [7] have been proposed to guide the search for excellent TE materials. The former results in the intensive studies on filled-skutterudites, clathrates, Zintl phases, and high-entropy alloys [8,9], while the latter pushes superionic chalcogenides to be hot, such as $(Ag,Cu)_2X$ (X = S, Se, and Te) [10] and argyrodite compounds ($A^{m+}_{(12-n)/m}B^{n+}X^{2-}_6$ (A = Li, Cu, and Ag; B = Ga, Si, Ge, Sn, P, and As; X = S, Se, and Te)) [11,12]. The most common characteristic of the superionic chalcogenides is that one relatively rigid sublattice formed by immobile ions and another liquid-like sublattice composed of mobile ions coexist in a crystal structure. The weak dependence between these two sublattices contributes to tunable electrical properties and low lattice thermal conductivity (κ_l) [10]. Among $(Ag,Cu)_2X$, AgCuTe-based materials own special evolution of the crystal structure, and then substantial and similar phase compositions could be achieved [13], providing additional freedom to manipulate the transport of electrons and phonons.

AgCuTe presents a phase transition at about 460 K with the increase of the temperature, from a complex hexagonal structure (space group: $P3m1$) to a cubic rocksalt phase (space group: $Fm\bar{3}m$), where Ag and Cu are like the melting state (disordered) and are caught by the face-centered cubic sublattice of Te atoms [14]. According to a pseudo-binary phase diagram of Ag_2Te and Cu_2Te, impurity phases belonging to Ag- and Cu-based tellurides are easy to be generated by manipulating the stoichiometric ratio below the phase transition temperature [15], and even small monoclinic Ag_2Te (space group: $P2_1/c$) exists in stoichiometric AgCuTe at room temperature. Because of Cu or/and Ag deficiency, intrinsic AgCuTe shows p-type TE materials, and its n always exceeds the optimized value. Besides, the high-temperature cubic phase with higher structural symmetry is demonstrated to exhibit superior TE performance than the low-temperature hexagonal phase, which may be due to the enhanced degeneracy of carrier pockets and softened chemical bonds. Therefore, inhibiting the generation of a cation vacancy and reducing the phase transition temperature were intensively adopted to improve TE properties of the AgCuTe-based materials. For example, alloying Se in a Te sublattice could be applied to both suppress the concentration of the cation vacancy and accelerate the hexagonal–cubic phase transition, elevating the peak zT values to above 1 [13,14,16,17]. I-doping and manipulation of the Ag : Cu ratio were also used to obtain a cubic structure at room temperature and decrease the cation vacancy, respectively [18–20]. However, tailoring the phase interface to decouple the transport of electrons and phonons has nearly never been noticed in the AgCuTe-based TE materials.

It is claimed that the phonon scattering in the TE materials could be greatly enhanced at the all-scale hierarchical architectures [21–23], including phase interface and grain boundary, but TE matrixes with small impurity phases were always constructed to scatter phonons without obviously disturbing the carriers in this common method. In this study, we demonstrate that a superior multiphase interface with simultaneous strong phonon scattering and weak electron scattering could be realized in the AgCuTe-based TE materials with considerable impurity phases (Ag_2Te, copper telluride (Cu_2Te and $Cu_{2-x}Te$), and nickel telluride (NiTe)). Furthermore, it has been reported that the Ni-doping at Cu sites in AgCuSe, which introduces chemical and lattice disorder, could enhance electron mobility and reduce κ_l. Motivated by this effect, the Ni-doping was also applied to optimize electrical and thermal parameters of AgCuTe, such as n and κ_l [24]. As a result, the power factor (PF = $S^2\sigma$) is significantly increased from ~609 to ~832 $\mu W \cdot m^{-1} \cdot K^{-2}$, and κ is synergistically reduced from ~0.52 to ~0.43 $W \cdot m^{-1} \cdot K^{-1}$ at 636 K in comparison with those of the reference sample, leading to a peak zT of ~1.23 at 636 K and an average zT (zT_{avg}) of ~1.12 in the temperature range of 523–623 K. This study provides a new approach to enhancing the TE properties by designing superior multiphase interfaces.

2 Experimental procedures

To synthesize the AgCuTe-based TE bulk materials

with multiphase compositions, we adopted a planetary ball milling method and a following spark plasma sintering (SPS) process. In detail, high-purity Ag (99.9%, Aladdin), Cu (99.9%, Aladdin), Te (99.9%, Aladdin), and Ni (99.9%, Aladdin) were weighted in a glovebox (Super, MIKROUNA, Germany) with the components of raw materials according to the molar ratio of Ag : Cu : Ni : Te =$[1 - 0.01(x + y)] : (1 + 0.01x) : (1 + 0.01y) : 1$. For the convenience of description, the name of the samples is abbreviated as S-*xy*. For example, the synthesized sample with the molar ratio of Ag : Cu : Ni : Te = 0.95 : 1.02 : 0.03 : 1 is represented by S-23. The weighted raw materials were sealed in stainless steel agate jars with an argon atmosphere. The agate jars were then rotated at a speed of 500 r·min^{-1} for 20 h in a planetary ball mill (WXQM-0.4L, Tencan Powder, China). After the ball milling process, the obtained powders were transferred into graphite molds with a diameter of 15 mm in the glovebox for the SPS process. At the beginning of the sintering process, the temperature rose rapidly from room temperature to 483 K with a speed of 100 K·min^{-1} and held at this temperature for 4 min. After that, the temperature increased further up to 673 K with a speed of 50 K·min^{-1} and held at this temperature for 3 min. Finally, the samples were cooled down to room temperature within 1 h, and the pressure was removed when the temperature dropped to 423 K. The obtained cylindrical alloy blocks with high relative densities were cut into suitable shapes for characterization of crystal structures, compositions, chemical states, and TE transport properties.

The crystal structures and phase compositions of all samples were characterized by an X-ray diffractometer (D8 Advance, Bruker, Germany) with Kα radiation (λ = 1.54 Å) at 40 kV and 40 mA. A transmission electron microscope (TEM; Talos F200X, FEI, USA) with its own patented and integrated energy dispersive spectrometer (EDS; Super-X, FEI, USA) with four silicon drift detectors (SDDs) was used to analyze the microstructure and elemental distribution. Chemical states of Ag, Cu, Ni, and Te were tested on an X-ray photoelectron spectrometer (Escalab 250Xi, ThermoFisher, USA). The phase transition was determined by a differential scanning calorimeter (DSC 404 F3, NETZSCH, Germany). For the test of electrical properties, the sintered bulks were cut into rectangular bars with a size of ~3 mm × 3 mm × 12 mm. The σ and S were measured by commercial equipment (CTA-3, Cryoall, China) in a low-helium-pressure atmosphere. The Hall carrier mobility (μ) and n were evaluated by van der Pauw method on a commercial Hall effect test system (Model 8404, Lakeshore, USA) with a reversible magnetic field up to 1.5 T according to the equation: $n = 1/(eR_H)$ and $\mu = \sigma R_H$, where R_H is the Hall coefficient, and e is the elementary charge. The κ was calculated by the equation: $\kappa = Dc_pd$, where D is the thermal diffusivity, d is the measured density, and c_p is the specific heat capacity. The D was tested under a low-pressure argon atmosphere with a commercial device (LFA 467H, NETZSCH, Germany) with a sample size of ~0.8 mm in thickness and ~12.7 mm in diameter. In this study, c_p was adopted by Dolung–Petit law approximation [17], and d was measured by Archimedes drainage method (Table S1 in the Electronic Supplementary Material (ESM)). TE property uncertainties are as follows: The uncertainty of σ and S is about 3%, and the uncertainty of D is about 6%. As a result, the uncertainty of the final zT is estimated to be about 15%.

3 Results and discussion

In general, interfacial thermal resistance (thermal boundary resistance) plays a significant role in blocking heat flow in solid materials, so that more phase interfaces would be beneficial for reducing κ_l in the TE materials [25]. However, the phase interfaces also always obviously scatter the carriers to result in low μ because of the existence of a potential barrier induced by the depletion region, which depends on grain size, n, and dielectric constant [26]. Figure 1 shows schematic diagrams of four types of carriers and phonons scattering at phase interfaces. The high potential barrier would lead to strong carrier scattering (Figs. 1(a) and 1(c)), and hence the phase interfaces with a negligible depletion region (a low potential barrier) (Figs. 1(b) and 1(d)) are in favor of good electrical properties. Under further consideration of phonon scattering, it is reasonable to conclude that more phase interfaces with a low potential barrier tend to achieve the decoupled carrier and phonon transport, resulting in better TE performance (Fig. 1(d)).

To construct these multiple-phase interfaces, we synthesized the AgCuTe-based TE materials by manipulating the composition. Figure 2(a) shows powder X-ray diffraction (XRD) patterns of the

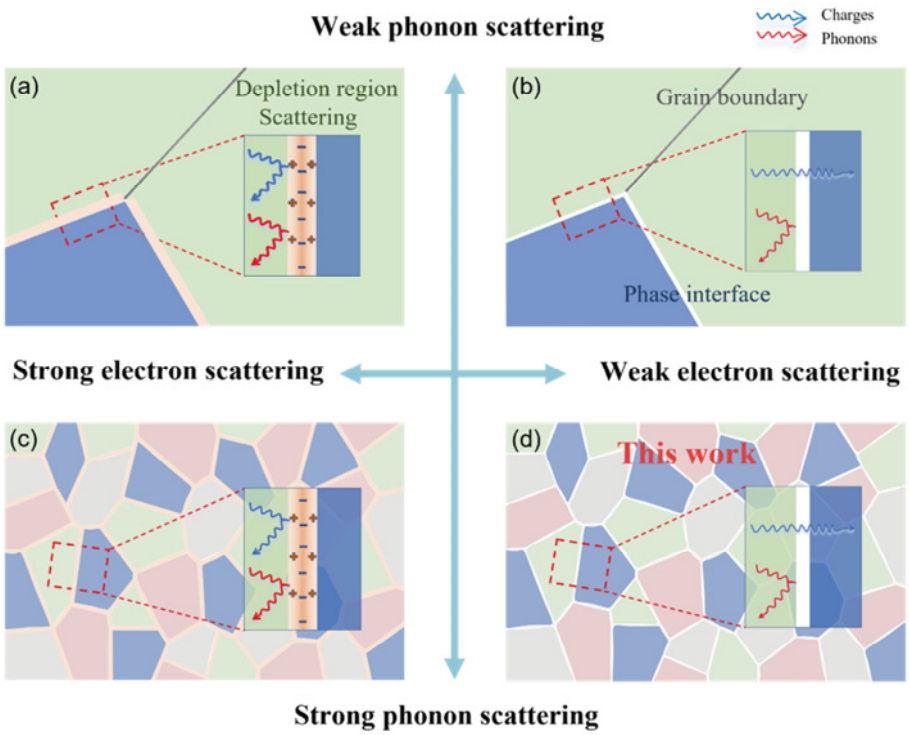

Fig. 1 Schematic illustration of phonons and carriers scattering at phase interface: (a) small interface with depletion regions to strongly scatter carriers but weakly scatter phonons, (b) small interface without depletion regions to weakly scatter both phonons and carriers, (c) large interface with depletion regions to strongly scatter both phonons and carriers, and (d) large interfaces without depletion regions to strongly scatter phonons but weakly scatter carriers.

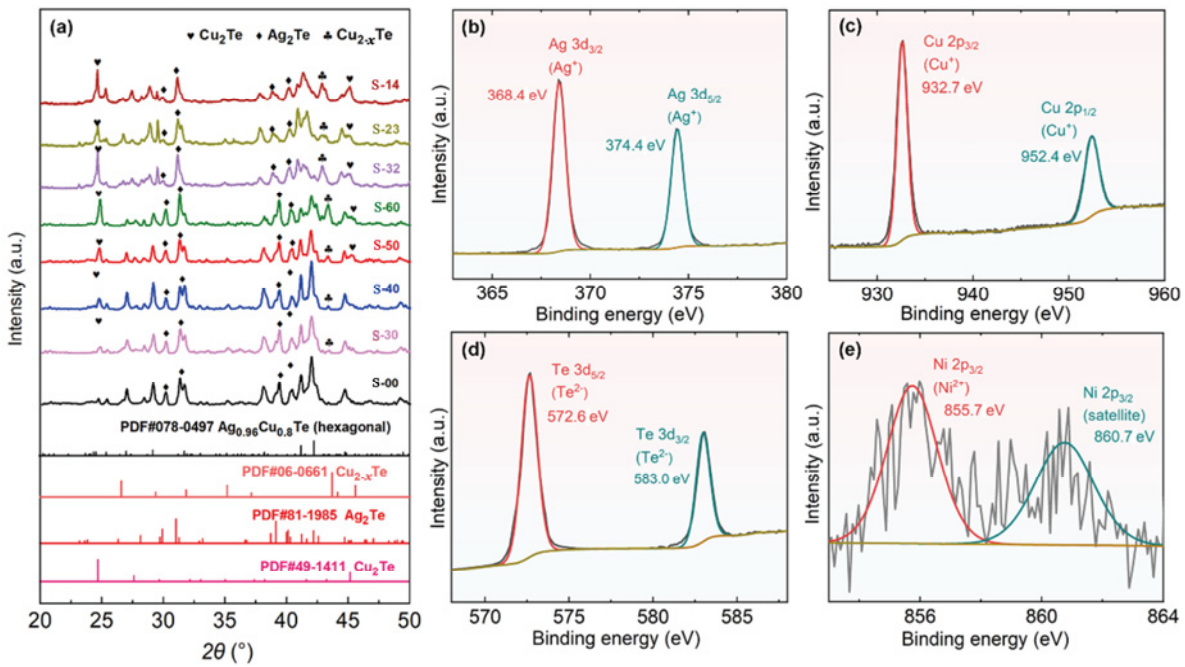

Fig. 2 (a) XRD patterns of as-prepared AgCuTe-based materials depending on Cu and Ni contents. XPS peaks of (b) Ag, (c) Cu, (d) Te, and (e) Ni.

as-prepared AgCuTe-based materials as a function of Cu and Ni contents. In Fig. 2(a), we can conclude that the main diffraction peaks could be ascribed to hexagonal AgCuTe (PDF#78-0497, space group: $P3m1$); meanwhile, there exists an obvious impurity phase of monoclinic Ag_2Te (PDF#81-1985, space group: $P2_1/c$) in the

pristine sample S-00. With the increase of the Cu content, two diffraction peaks at about 24.7° and 43.7° become more and more obvious, which could be matched with hexagonal Cu_2Te (PDF#49-1411, space group: *P*3*m*1) and tetragonal $Cu_{2-x}Te$ (PDF#06-0661, space group: *P*4/*nmm*), respectively. This phenomenon indicates that the compounds of Ag_2Te, Cu_2Te, and $Cu_{2-x}Te$ are easily generated by regulating the molar ratio of Cu and Ag. After the Ni-doping, the diffraction peaks of hexagonal AgCuTe, monoclinic Ag_2Te, hexagonal Cu_2Te, and tetragonal $Cu_{2-x}Te$ also could be identified, though there are slight changes in the peak shape and shifts of the peak position, possibly due to the influence of Ni performed on the local crystal lattice (e.g., the changes in the cation vacancy and Ni substitution at cation cites). Because of the low addition of Ni (the molar ratio of Ni : (Ag + Cu) is no more than 2%), XRD may no longer be credible in detecting impurity phases of NiTe according to its sensitivity. To reveal chemical states of Ag, Cu, Ni, and Te, X-ray photoelectron spectroscopy (XPS) analysis was performed on the sample S-23. As shown in Fig. 2(b), the peaks of binding energy at about 368.4 and 374.4 eV could be indexed to Ag $3d_{3/2}$ and Ag $3d_{5/2}$ with a chemical valence of +1, respectively [27]. Similarly, the chemical valences of Cu and Te are +1 and −2, respectively. The former is indicated by the peaks at about 932.7 eV (Cu $2p_{3/2}$) and 952.4 eV (Cu $2p_{1/2}$) (Fig. 2(c)) [28], while the latter is claimed by the peaks at about 572.6 eV (Te $3d_{5/2}$) and 583.0 eV (Te $3d_{3/2}$) (Fig. 2(d)) [27]. Besides, a weak peak at about 855.7 eV belonging to Ni $2p_{3/2}$ with +2 valence and its satellite peak at about 860.7 eV could be detected (Fig. 2(e)) [29], suggesting the existence of Ni.

TEM observation and EDS analysis are further applied to characterize crystal structure, microstructure, and phase composition. Figure 3(a) shows an image of the sample S-23 collected by a high-angle annular dark-field scanning transmission electron microscope (HAADF-STEM; Talos F200X, FEI, USA), where the intensity of the image depends on the atomic number (*Z*) of the element. It is obvious that the elemental distribution is not uniform because the image shows clear black-and-white contrasts in different regions, suggesting that the sample is a composite; this is in line with the result of XRD. With the aid of elemental mappings detected by EDS (Figs. 3(b)–3(e)), the elemental distribution becomes clearer, and hence the phase composition could be deduced. In detail, the matrix is mainly composed of Ag, Cu, and Te, corresponding to the information of the AgCuTe compound. Besides, a rodlike region (marked by "1" in Fig. 3(e)) with a size of about ~50 nm × 150 nm is very distinguishable, which mainly contains Te and Ni, indicating that this region should be NiTe. Meanwhile, Cu_2Te and $Cu_{2-x}Te$ could also be confirmed by the regions (marked by "2" in Fig. 3(c)), where Cu and Te are enriched, but Ag and Ni are missing. Last but not least, some nano-precipitates with a diameter below ~30 nm are most likely to form in the AgCuTe matrix. The black in the HAADF-STEM image due to smaller *Z* and deficiency of Ag and Te in elemental mappings demonstrate that they may be Cu- or Ni-enriched precipitates. Crystal structures of these compounds are characterized by the high-resolution TEM (HRTEM). In NiTe, a rhombohedral structure (space group: $R\bar{3}m$) of NiTe could be identified (Figs. 3(f) and 3(g) and the inset of Fig. 3(g)). Moiré fringes could be observed around the phase interface between the NiTe nano-precipitates and the AgCuTe matrix (Fig. 3(f)), which usually means the overlap of these two phases [30]. In addition, hexagonal Cu_2Te (Fig. 3(h) and the inset of Fig. 3(h)), monoclinic Ag_2Te (Fig. 3(i) and the inset of Fig. 3(i)), tetragonal $Cu_{2-x}Te$ (Fig. S1 in the ESM), and their phase interfaces with the AgCuTe matrix are also confirmed. It is believed that these phase interfaces could act as phonon scattering centers to reduce κ_l because the phase (grain) boundary could be considered as equivalent to dislocation (Figs. 3(j) and 3(k)) [31]. Besides, there are considerable stacking faults in the sample, as revealed by a linear feature in a fast Fourier transformation (FFT) pattern (Fig. 3(l)), which may also contribute to the enhanced phonon scattering [22]. In a word, there are multiple and complex phase compositions in the synthesized AgCuTe-based materials, which mainly consist of AgCuTe, Cu_2Te, $Cu_{2-x}Te$, Ag_2Te, and NiTe.

The phase transition is another parameter affecting the TE properties, which is measured by a differential scanning calorimetry (DSC) method. DSC curves exhibit that there are two main endothermic peaks near 414 and 504 K, which could be ascribed to the phase transition of Ag_2Te from monoclinic to cubic structures and AgCuTe from hexagonal to cubic phases, respectively (Fig. S2 in the ESM) [32,33]. The *in-situ* XRD patterns at variable temperatures also confirm the phase transition. As shown in Fig. S3 in the ESM, XRD patterns show an obvious variation from 500

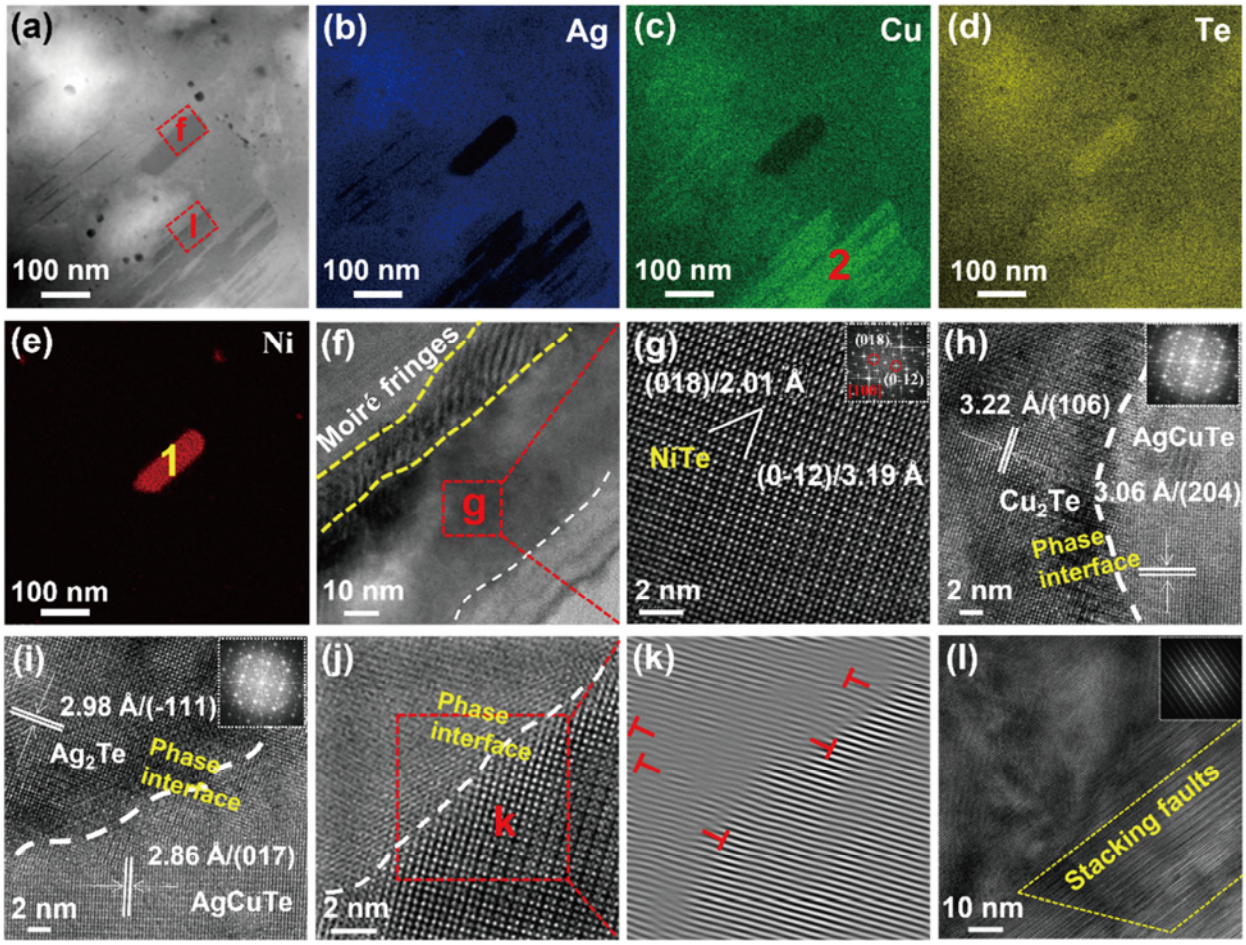

Fig. 3 (a) HAADF-STEM image of sample S-23 and its elemental mappings: (b) Ag, (c) Cu, (d) Te, and (e) Ni. (f) Enlarged bright field (BF) image on the region marked by "f" in (a). (g) HRTEM image on the region marked by "g" in (f); the inset is its corresponding FFT pattern. HRTEM images focusing on phase interfaces between (h) Cu_2Te and AgCuTe and (i) Ag_2Te and AgCuTe; the insets are their corresponding FFT patterns. (j) HRTEM image and (k) its corresponding inverse FFT pattern. (l) HRTEM image on the region marked by "l" in (a); the inset is its corresponding FFT pattern.

to 600 K, where the diffraction peaks collected at 600 K could be mainly ascribed to cubic AgCuTe and hexagonal Cu_2Te, indicating the phase transition of AgCuTe from hexagonal to cubic phases ($Fm\bar{3}m$). Furthermore, it seems that the Ni-doping induces ignorable effect on the phase transition temperature. Therefore, it is reasonable to conclude that n and phase interfaces would mainly dominate the TE properties.

Figure 4 and Fig. S4 in the ESM show electrical properties of the as-prepared AgCuTe-based materials with different Cu and Ni contents. The σ of all samples decrease with the rise of the temperature below about 500 K, suggesting electron transport behavior of degenerated semiconductors (Fig. 4(a) and Fig. S4(a) in the ESM). In contrast, σ displays negligible temperature dependence above 500 K. This could be explained by the phase transition, as exposed by a DSC measurement. Above 500 K, the samples are superionic conductors, and thus show weak temperature dependence in the electrical properties, which is also always observed in Refs. [16,17,34]. In addition, σ decreases in the whole temperature range as the Cu content increases and is further reduced by the Ni-doping. For example, σ at 636 K is ~3.67×10^4 S·m^{-1} in the reference sample S-00, being depressed to ~2.81×10^4 S·m^{-1} in the sample S-50, and further reduced to ~1.50×10^4 S·m^{-1} in the sample S-23 by the Ni-doping. On the other hand, the changing trend of S as a function of the temperature and the contents of Cu and Ni are opposite to those of σ (Fig. 4(b) and Fig. S4(b) in the ESM), leading to the enhancement of S from ~128 μV·K^{-1} in the sample S-00 to ~247 μV·K^{-1} in the sample S-23 at 636 K. According to Eqs. (1) and (2) [4],

$$\sigma = ne\mu \quad (1)$$

$$S = \frac{8\pi^2 k_B^2}{3eh^2} m^* T \left(\frac{\pi}{3n}\right)^{2/3} \quad (2)$$

where k_B is the Boltzmann constant, h is the Planck constant, and m^* is the density of the state effective mass; the decrease in σ and increase in S with the increasing contents of Cu and Ni are most likely to be introduced by the reduction of n. We obtained n and μ by Hall effect measurement at 300 K (Fig. 4(c)). As expected, n is suppressed by the Ni-doping from ~4.50×10^{19} cm^{-3} in the sample S-50 to ~1.82×10^{19} cm^{-3} in the sample S-14. This may be due to the depressed formation of the cationic vacancy [14] or the replacement of Ni ions with a higher chemical valence (+2) at Cu or Ag ion cites with a lower chemical valence (+1) as electron donors. Pisarenko plot based on a single parabolic band (SPB) model under acoustic phonon scattering provides the relation between n and S at 300 K (Section S1 in the ESM) [35], which demonstrates that m^* of the Ni-doped samples is about $0.24m_e$ (m_e is the electron effective mass), and it seems to have nothing to do with the content of Ni (Fig. S5 in the ESM). Correspondingly, μ is increased from ~112.5 cm^2·V^{-1}·s^{-1} (S-50) to ~210.3 cm^2·V^{-1}·s^{-1} (S-14) by the Ni-doping, indicating that the carrier scattering at the phase interfaces and the ionized impurity scattering induced by Ni substitutional doping in crystals are very weak. This may be due to the negligible depletion region at the phase interface induced by the similar chemical bonds in transition-metal tellurides [36]. Thanks to enhanced S in the whole temperature range, PF is accordingly enhanced by the addition of Cu and Ni (Fig. 4(d)). For instance, PF at 636 K in the sample S-00 is ~609 μW·m^{-1}·K^{-2}, which is increased to ~832 μW·m^{-1}·K^{-2} in the sample S-23.

As shown in Fig. 5(a) and Fig. S6(a) in the ESM, κ of all samples present a drop below 500 K but a rise above 500 K with the increasing temperature. Similar to the explanation in the electrical properties, the changing trend in κ should be related to the phase transition. In other words, the origin of conducting heat in a low-temperature phase differs from that in a high-temperature superionic phase. Apart from the influence of the temperature, the increase of the Cu content contributes to slightly promote κ, while the Ni-doping acts as an opposite effect in the whole temperature range, so that κ is reduced from ~0.52 W·m^{-1}·K^{-1} (S-00) to ~0.43 W·m^{-1}·K^{-1} (S-23) at 636 K. To analyze the phonon scattering mechanism, we calculated κ_l by subtracting κ_e (Fig. S6(b) in the ESM) from κ, where κ_e is estimated by Wiedemann–Franz law: $\kappa_e = L\sigma T$ (the Lorentz number (L) is obtained by the SPB model with acoustic phonon scattering) [35]. Owing to the reduction of σ, κ_e is

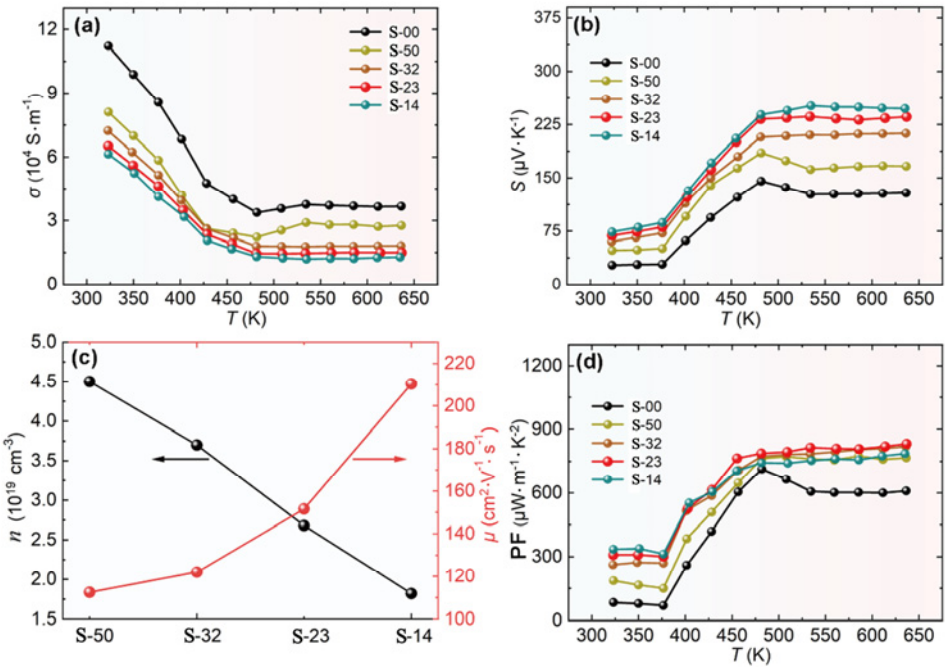

Fig. 4 (a) σ and (b) S of as-prepared samples as a function of temperature. (c) n and μ of samples S-50, S-32, S-23, and S-14 at 300 K. (d) PF of synthesized samples depending on temperature.

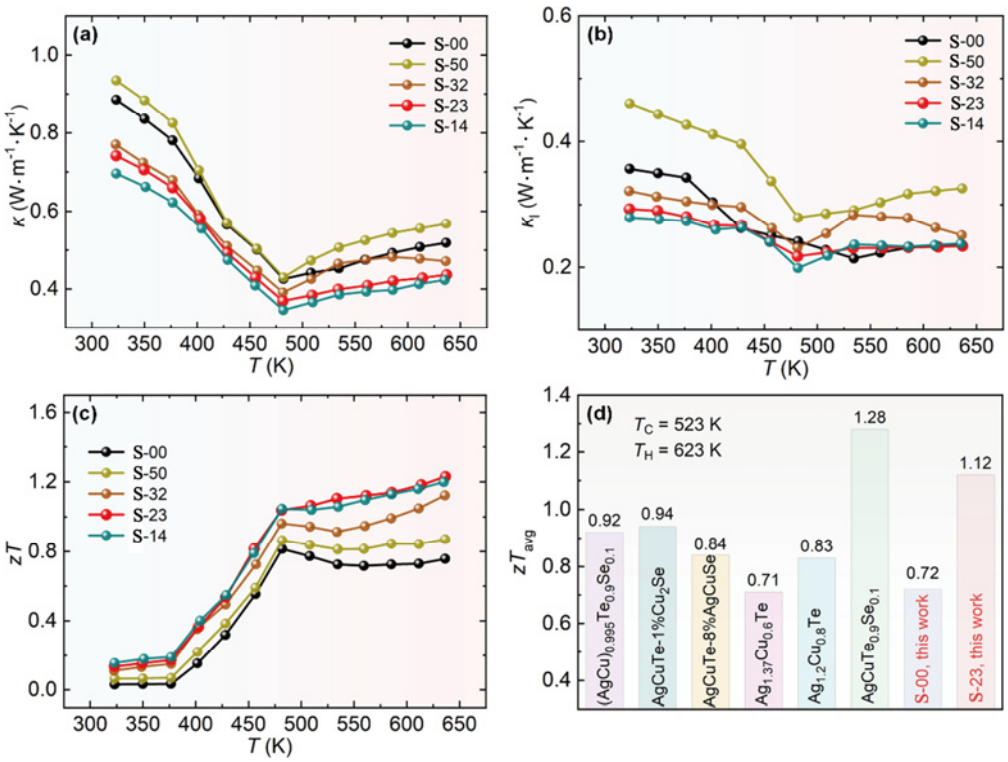

Fig. 5 (a) κ, (b) κ_l, and (c) zT of as-prepared samples as a function of temperature. (d) zT_{avg} of samples S-00 and S-23 in temperature range of 523–623 K and in contrast with those reported in Refs. [13,16,17,20,33,34] where T_C and T_H are the temperatures of cold and hot ends, respectively.

obviously decreased in the whole temperature range by the addition of Cu and Ni. However, the increase of the Cu content boosts the transport of phonons, resulting in the enhancement of κ_l in the sample S-50 (~0.33 $W \cdot m^{-1} \cdot K^{-1}$ at 636 K) (Fig. 5(b)). This may be due to the formation of Cu_2Te and $Cu_{2-x}Te$ impurity phases by the addition of Cu, which owns higher κ_l than that of the AgCuTe matrix. Fortunately, the Ni-doping significantly decreases κ_l to ~0.43 $W \cdot m^{-1} \cdot K^{-1}$ at 636 K for the sample S-23, which may be attributed to the enhanced phonon scattering induced by the microstructures (e.g., dislocation and stacking faults) at the multiphase interfaces, as observed by the TEM characterization because mass and strain field fluctuations induced by the Ni substitutional doping are not enough to contribute the observed reduction of κ_l based on Debye–Callaway model (Section S2 and Fig. S7 in the ESM). It is also worth noting that the changing trend in the low-temperature phases has higher temperature dependence than that in the high-temperature superionic phases. This is to be expected because the weak temperature dependence in κ_l is always tested in the superionic conductors [10,17].

Because of the simultaneous enhancement in PF and reduction in κ, the great improvement in zT is achieved (Fig. 5(c)). Finally, a peak zT of ~1.23 at 636 K and zT_{avg} of ~1.12 in the temperature range of 523–623 K are obtained in the sample S-23 (Fig. 5(d)), which have an about 50% enhancement in comparison with those of the sample S-00 and are both one of the best values among the AgCuTe-based TE materials [13,16,17, 20,33,37].

4 Conclusions

In summary, we successfully synthesized AgCuTe-based TE materials with multiphase compositions by the planetary ball milling technique and the following SPS process. The XRD and TEM results demonstrate that the as-prepared samples own the AgCuTe matrix and contain considerable and complex impurity phases mainly composed of Ag_2Te, Cu_2Te, $Cu_{2-x}Te$, and NiTe. The generated multiphase interfaces synergistically optimize the transport of electrons and phonons with weak scattering for the former but strong scattering for the latter, so that PF is obviously increased from ~609 to ~832 $\mu W \cdot m^{-1} \cdot K^{-2}$, and κ is reduced from ~0.52 to ~0.43 $W \cdot m^{-1} \cdot K^{-1}$ at 636 K, in contrast with those of pristine AgCuTe (S-00). This superior effect at the

phase interfaces is most likely to be contributed by the similar chemical bonds in these transition-metal tellurides. Finally, a peak zT of ~1.23 at 636 K and a zT_{avg} of ~1.12 in the temperature range of 523–623 K are achieved in the sample S-23, which are both one of the best values among the AgCuTe-based TE materials. It is expected that this study would give potential instruction to construct a superior phase interface in other TE materials.

Acknowledgements

This work is supported by the National Natural Science Foundation of China (Grant Nos. 52262032, 52273285, 51961011, 52061009, and U21A2054) and the National Key R&D Program of China (Grant No. 2022YFE0119100).

Declaration of competing interest

The authors have no competing interests to declare that are relevant to the content of this article.

Electronic Supplementary Material

Supplementary material is available in the online version of this article at https://doi.org/10.26599/JAC.2023.9220768.

References

[1] Shi XL, Zou J, Chen ZG. Advanced thermoelectric design: From materials and structures to devices. *Chem Rev* 2020, **120**: 7399–7515.

[2] Zheng ZH, Li YL, Niu JY, *et al*. Significantly (00*l*)-textured Ag_2Se thin films with excellent thermoelectric performance for flexible power applications. *J Mater Chem A* 2022, **10**: 21603–21610.

[3] Yan QY, Kanatzidis MG. High-performance thermoelectrics and challenges for practical devices. *Nat Mater* 2022, **21**: 503–513.

[4] Liu CY, Huang ZW, Wang DH, *et al*. Dynamic Ag^+-intercalation with $AgSnSe_2$ nano-precipitates in Cl-doped polycrystalline $SnSe_2$ toward ultra-high thermoelectric performance. *J Mater Chem A* 2019, **7**: 9761–9772.

[5] Jia N, Tan XY, Xu JW, *et al*. Achieving enhanced thermoelectric performance in multiphase materials. *Acc Mater Res* 2022, **3**: 237–246.

[6] Slack GA, Rowe DM. *CRC Handbook for Thermoelectrics*. Boca Raton, USA: CRC Press, 1995.

[7] Liu HL, Shi X, Xu FF, *et al*. Copper ion liquid-like thermoelectrics. *Nat Mater* 2012, **11**: 422–425.

[8] Sootsman JR, Chung DY, Kanatzidis MG. New and old concepts in thermoelectric materials. *Angew Chem Int Ed* 2009, **48**: 8616–8639.

[9] Jiang BB, Wang W, Liu SX, *et al*. High figure-of-merit and power generation in high-entropy GeTe-based thermoelectrics. *Science* 2022, **377**: 208–213.

[10] Zhao KP, Qiu PF, Shi X, *et al*. Recent advances in liquid-like thermoelectric materials. *Adv Funct Mater* 2020, **30**: 1903867.

[11] Yu ZH, Wang XX, Liu CY, *et al*. Carrier and microstructure tuning for improving the thermoelectric properties of Ag_8SnSe_6 via introducing $SnBr_2$. *J Adv Ceram* 2022, **11**: 1144–1152.

[12] Wang XX, Liu CY, Chen JL, *et al*. Synergistically optimizing the thermoelectric properties of polycrystalline Ag_8SnSe_6 by introducing additional Sn. *CrystEngComm* 2020, **22**: 248–256.

[13] Li LW, Zhai WY, Wang C, *et al*. Maximizing phonon scattering efficiency by Cu_2Se alloying in AgCuTe thermoelectric materials. *J Mater Chem A* 2022, **10**: 6701–6712.

[14] Roychowdhury S, Jana MK, Pan J, *et al*. Soft phonon modes leading to ultralow thermal conductivity and high thermoelectric performance in AgCuTe. *Angew Chem Int Ed* 2018, **57**: 4043–4047.

[15] Chang YA, Goldberg D, Neumann JP. Phase diagrams and thermodynamic properties of ternary copper–silver systems. *J Phys Chem Ref Data* 1977, **6**: 621–674.

[16] Deng SP, Jiang XY, Chen LL, *et al*. Ultralow thermal conductivity and high thermoelectric performance in $AgCuTe_{1-x}Se_x$ through isoelectronic substitution. *ACS Appl Mater Interfaces* 2021, **13**: 868–877.

[17] Jiang J, Zhu HT, Niu Y, *et al*. Achieving high room-temperature thermoelectric performance in cubic AgCuTe. *J Mater Chem A* 2020, **8**: 4790–4799.

[18] Niu Y, Li S, Mao J, *et al*. Suppressed phase transition and enhanced thermoelectric performance in iodine-doped AgCuTe. *Nano Energy* 2020, **77**: 105297.

[19] Ballikaya S, Chi H, Salvador JR, *et al*. Thermoelectric properties of Ag-doped Cu_2Se and Cu_2Te. *J Mater Chem A* 2013, **1**: 12478–12484.

[20] Zhu HT, Luo J, Zhao HZ, *et al*. Enhanced thermoelectric properties of p-type Ag_2Te by Cu substitution. *J Mater Chem A* 2015, **3**: 10303–10308.

[21] Zhao LD, Dravid VP, Kanatzidis MG. The panoscopic approach to high performance thermoelectrics. *Energy Environ Sci* 2014, **7**: 251–268.

[22] Zheng YY, Liu CY, Miao L, *et al*. Extraordinary thermoelectric performance in MgAgSb alloy with ultralow thermal conductivity. *Nano Energy* 2019, **59**: 311–320.

[23] Zhao WY, Liu ZY, Sun ZG, *et al*. Superparamagnetic enhancement of thermoelectric performance. *Nature* 2017, **549**: 247–251.

[24] Ishiwata S, Shiomi Y, Lee JS, *et al*. Extremely high electron mobility in a phonon-glass semimetal. *Nat Mater* 2013, **12**: 512–517.

[25] Chen J, Xu XF, Zhou J, *et al*. Interfacial thermal resistance: Past, present, and future. *Rev Mod Phys* 2022, **94**: 025002.
[26] Hu CL, Xia KY, Fu CG, *et al*. Carrier grain boundary scattering in thermoelectric materials. *Energy Environ Sci* 2022, **15**: 1406–1422.
[27] Samal AK, Pradeep T. Room-temperature chemical synthesis of silver telluride nanowires. *J Phys Chem C* 2009, **113**: 13539–13544.
[28] Qian K, Gao L, Li H, *et al*. Epitaxial growth and air-stability of monolayer Cu_2Te. *Chinese Phys B* 2020, **29**: 018104.
[29] Yuan ML, Li QG, Zhang JX, *et al*. Engineering surface atomic architecture of NiTe nanocrystals toward efficient electrochemical N_2 fixation. *Adv Funct Mater* 2020, **30**: 2004208.
[30] Ke XX, Zhang MC, Zhao KN, *et al*. Moiré fringe method via scanning transmission electron microscopy. *Small Methods* 2022, **6**: 2101040.
[31] Kim HS, Kang SD, Tang YL, *et al*. Dislocation strain as the mechanism of phonon scattering at grain boundaries. *Mater Horiz* 2016, **3**: 234–240.
[32] Fujikane M, Kurosaki K, Muta H, *et al*. Electrical properties of α- and β-Ag_2Te. *J Alloys Compd* 2005, **387**: 297–299.
[33] Zhu WM, Huang ZY, Chu MH, *et al*. Enhanced thermoelectric performance through optimizing structure of anionic framework in AgCuTe-based materials. *Chem Eng J* 2020, **386**: 123917.
[34] Zhang BG, Yang H, Tian Z, *et al*. Effect of Ni doping on thermoelectric properties of Ag_2Te–Cu_2Te composite material. *J Alloys Compd* 2021, **870**: 159425.
[35] Zhu JB, Zhang XM, Guo MC, *et al*. Restructured single parabolic band model for quick analysis in thermoelectricity. *npj Comput Mater* 2021, **7**: 116.
[36] Wu XZ, Han ZJ, Zhu YB, *et al*. A general design strategy for thermoelectric interface materials in n-type $Mg_3Sb_{1.5}Bi_{0.5}$ single leg used in TEGs. *Acta Mater* 2022, **226**: 117616.
[37] Wu RN, Li ZL, Li YB, *et al*. Synergistic optimization of thermoelectric performance in p-type Ag_2Te through Cu substitution. *J Materiomics* 2019, **5**: 489–495.